


# Soft and MRI Compatible Neural Electrodes from Carbon Nanotube Fibers

Linlin Lu,<sup>†,‡</sup> Xuefeng Fu,<sup>†</sup> Yijun Liew,<sup>‡</sup> Yongyi Zhang,<sup>§</sup> Siyuan Zhao,<sup>†,||</sup> Zheng Xu,<sup>†</sup> Jingna Zhao,<sup>§</sup> Da Li,<sup>§</sup> Qingwen Li,<sup>§</sup> Garrett B. Stanley,<sup>\*,‡</sup> and Xiaojie Duan<sup>\*,†,||</sup> 

<sup>†</sup>Department of Biomedical Engineering, College of Engineering, Peking University, Beijing 100871, China

<sup>‡</sup>Wallace H. Coulter Department of Biomedical Engineering, Georgia Institute of Technology and Emory University, Atlanta, Georgia 30332, United States

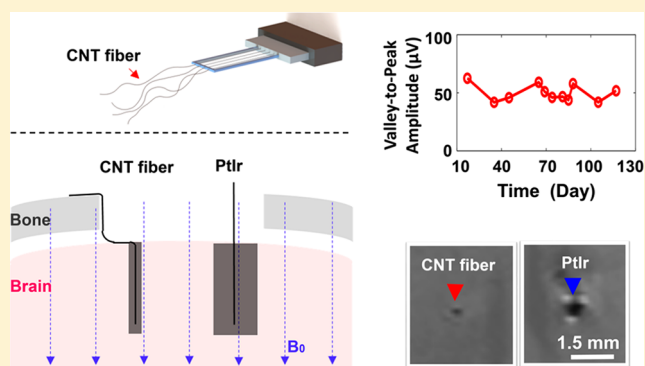
<sup>§</sup>Suzhou Institute of Nano-Tech and Nano-Bionics (SINANO), Chinese Academy of Sciences, Suzhou 215123, China

<sup>||</sup>Academy for Advanced Interdisciplinary Studies, Peking University, Beijing 100871, China

**S** Supporting Information

**ABSTRACT:** Soft and magnetic resonance imaging (MRI) compatible neural electrodes enable stable chronic electrophysiological measurements and anatomical or functional MRI studies of the entire brain without electrode interference with MRI images. These properties are important for many studies, ranging from a fundamental neurophysiological study of functional MRI signals to a chronic neuromodulatory effect investigation of therapeutic deep brain stimulation. Here we develop soft and MRI compatible neural electrodes using carbon nanotube (CNT) fibers with a diameter from 20  $\mu\text{m}$  down to 5  $\mu\text{m}$ . The CNT fiber electrodes demonstrate excellent interfacial electrochemical properties and greatly reduced MRI artifacts than PtIr electrodes under a 7.0 T MRI scanner. With a shuttle-assisted implantation strategy, we show that the soft CNT fiber electrodes can precisely target specific brain regions and record high-quality single-unit neural signals. Significantly, they are capable of continuously detecting and isolating single neuronal units from rats for up to 4–5 months without electrode repositioning, with greatly reduced brain inflammatory responses as compared to their stiff metal counterparts. In addition, we show that due to their high tensile strength, the CNT fiber electrodes can be retracted controllably postinsertion, which provides an effective and convenient way to do multidepth recording or potentially selecting cells with particular response properties. The chronic recording stability and MRI compatibility, together with their small size, provide the CNT fiber electrodes unique research capabilities for both basic and applied neuroscience studies.

**KEYWORDS:** *Neural chronic recording, brain implants, minimal neuroinflammation, brain–machine interface, nanobioelectronics, whole-brain mapping, multimodal neural interfacing*



Magnetic resonance imaging (MRI) compatible neural electrodes enable anatomical and functional MRI studies across entire brain regions without electrode interference with the imaging.<sup>1,2</sup> This is important for combining high-resolution electrophysiological measurements and global MRI brain activity mapping for neuroscience studies.<sup>3,4</sup> Many applications, such as verification of placement and stability of implanted electrodes, localization of epileptic foci, neurophysiological study of functional MRI (fMRI) signals, and brain circuit activation pattern mapping with simultaneous fMRI and deep brain stimulation (DBS), can greatly benefit from using MRI compatible neural electrodes.<sup>2,3,5</sup> Current implantable neural stimulating or recording electrodes are mainly made of noble metals, stainless steel, and crystalline silicone, etc.<sup>6</sup> These materials usually possess good stability and interfacial electrochemical characteristics. How-

ever, even if nonferromagnetic, they may induce severe field distortions and cause large image artifacts or blind areas around the electrodes in MRI,<sup>1</sup> making it impossible to visualize the surrounding brain tissues.

We have recently reported an MRI compatible implantable neural recording electrode using a graphene encapsulated copper (G-Cu) microwire.<sup>1</sup> The G-Cu microelectrodes exhibit artifact-free properties under 7.0 T MRI scans, which is attributed to the close magnetic susceptibility between copper and water/tissues. However, like other stiff implantable neural electrodes,<sup>7–9</sup> G-Cu microelectrodes elicit a sustained inflammation and tissue response over time and eventually

**Received:** November 5, 2018

**Revised:** February 3, 2019

**Published:** February 24, 2019

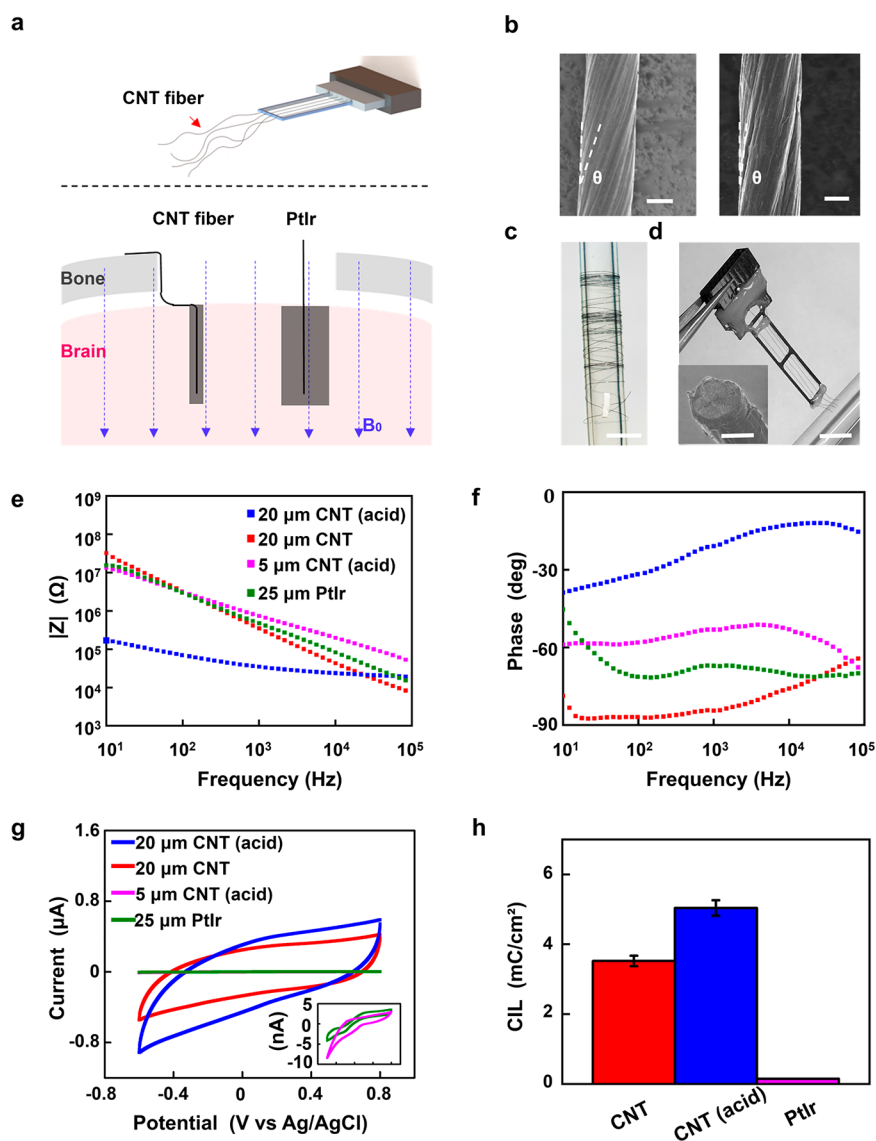


**Figure 1.** Characterization of CNT fiber electrodes. (a) Schematic drawing of the soft and MRI compatible CNT fiber electrodes. The gray shadow around the implanted CNT fiber and PtIr electrodes illustrates the MRI artifact. (b) SEM images of the side view of  $\sim 20$   $\mu\text{m}$  (left, scale bar, 10  $\mu\text{m}$ ) and  $\sim 5$   $\mu\text{m}$  (right, scale bar, 2  $\mu\text{m}$ ) diameter CNT fibers used in this study. The twisting angle is indicated as  $\theta$ . (c) Picture of an  $\sim 15$   $\mu\text{m}$  diameter CNT fiber insulated with  $\sim 2.5$   $\mu\text{m}$  Parylene-C wrapped on a Teflon tube. Scale bar, 5 mm. (d) Picture of a four-channel CNT fiber microelectrode assembly. Scale bar, 5 mm. Inset, SEM image of a CNT fiber electrode tip. Scale bar, 10  $\mu\text{m}$ . (e–g) Impedance magnitude (e), phase (f), and CV (g) of electrodes made of 20  $\mu\text{m}$  diameter CNT fibers treated with and without nitric acid, 5  $\mu\text{m}$  CNT fibers treated with nitric acid, and 25  $\mu\text{m}$  PtIr wires. The same color codes in panel e are used in panel f. (h) Charge injection limit of electrodes made from CNT fibers treated with and without nitric acid and PtIr. Error bars show SEM ( $n = 8$ ).

lead to neuronal degradation and glial scar formation near the implants, which causes degradation of function over chronic implantation. It is believed that, under mechanical mismatch between the stiff electrodes and brain tissues, the natural micromotion of the host brain tissue induces intense stress at the electrode–brain interface, leading to repetitive mechanical stimulation and injury, which results in this chronic inflammatory response.<sup>7,10</sup> Recent research efforts have demonstrated that increasing the softness and decreasing the size of the neural electrodes reduces chronic neuronal degradation and formation of a glial scar, thus improving the stability of the neural interface.<sup>11–14</sup> Ultrathin-polymer-film-based electrodes with bending stiffness comparable to that of the brain tissues have been demonstrated to form glial scar-free neural integration,<sup>12–14</sup> which allowed for stable tracking of the

same individual neurons on a months-to-year time scale.<sup>13</sup> These studies support the validity of using soft and ultrasmall implantable electrodes for chronically stable neural activity mapping and modulation.

In this work, we set out to develop a soft and MRI compatible implantable electrode for use in chronic longitudinal studies employing both MRI and electrophysiology. A carbon nanotube (CNT) microfiber was utilized as the electrode material due to its high softness and close magnetic susceptibility between CNT and water/tissues. In a previous study, CNT fiber microelectrodes were demonstrated to possess remarkable electrochemical properties including low impedance and high charge injection capacity.<sup>15</sup> Here we fabricated neural electrodes from CNT fibers with a diameter from 20  $\mu\text{m}$  down to 5  $\mu\text{m}$  (total electrode diameter from 25

$\mu\text{m}$  down to  $10\ \mu\text{m}$ ), which have bending stiffness orders of a magnitude smaller than the values reported for previous implantable electrodes, such as silicon or carbon fiber electrodes.<sup>11,12,16</sup> We show that the soft CNT fiber electrodes elicit greatly reduced inflammatory responses compared to PtIr electrodes of a similar size and can detect and isolate single-unit neural signals for up to 4–5 months without electrode repositioning. The MRI studies of rats implanted with CNT fiber electrodes in a high-field 7.0 T scanner indicate that the CNT fiber electrodes show a greatly reduced artifact than the PtIr electrodes, indicating less magnetic field distortion in their vicinity.

The CNT fibers used for neural microelectrode fabrication were spun by drawing and twisting CNT strips out of a vertically aligned array of CNTs, which consists of double- and triple-walled CNTs with diameters of  $\sim 6\ \text{nm}$ , with the assistance of ethanol infiltration.<sup>17</sup> This yields CNT fibers with a high electrical conductivity, tensile strength, and flexibility. The diameter of the CNT fiber is mainly determined and controlled by the width of the CNT array used for spinning. In addition, the twisting angle can also influence the electrical conductivity and mechanical properties of the CNT fibers.<sup>18</sup> Representative scanning electron microscopy (SEM) images of a  $\sim 20$  and  $\sim 5\ \mu\text{m}$  diameter CNT fiber with a twisting angle of  $\sim 18^\circ$  and  $\sim 5^\circ$ , respectively, used in this study are shown in Figure 1b. The electrode fabrication started with insulating individual CNT fibers with an  $\sim 2.5\ \mu\text{m}$  thick layer of Parylene-C film. After we soldered one end of the CNT fibers to metal connectors used to interface with the preamplifier, the insulated CNT fibers were cut mechanically to expose the cross sections as electrically active recording or stimulating sites. A picture of an insulated CNT fiber wrapping around a Teflon tube (Figure 1c) and a four-channel CNT fiber microelectrode array (Figure 1d) shows that the CNT fibers can be easily bent, which is not possible for PtIr electrodes or carbon fiber electrodes of a similar size. The exposed cross sections of the CNT fiber electrodes (inset, Figure 1d) exhibited a loose and porous microstructure, which resulted in a large surface area and is advantageous for achieving a high charge injection capacity and low impedance.

Electrochemical impedance spectroscopy (EIS) measurements (Figure 1e,f) gave an impedance value of  $279.96 \pm 32.08\ \text{k}\Omega$  (mean  $\pm$  SEM,  $n = 8$ ) at 1 kHz for electrodes made from CNT fibers with a diameter of  $20\ \mu\text{m}$ . Nitric acid treatment of CNT fibers decreased the impedance to  $41.95 \pm 3.62\ \text{k}\Omega$  (mean  $\pm$  SEM,  $n = 8$ ) at 1 kHz. (See the Experimental Section for details.) This value is  $\sim 9$  times lower than that of PtIr electrodes of a similar size ( $367.73 \pm 52.21\ \text{k}\Omega$  at 1 kHz, mean  $\pm$  SEM,  $n = 8$ , PtIr wire diameter of  $25\ \mu\text{m}$ ). Nitric acid treatment is known to increase the electrical conductivity of the CNT fibers by doping and decreasing the cross-junction resistance due to the removal of impurities.<sup>19</sup> The removal of impurities in interstitial spaces between the aligned CNTs can also increase the surface area accessible to ions. All of these could account for the reduced impedance of the CNT fiber electrodes. The cyclic voltammogram (CV) of the CNT fiber electrodes showed a featureless nonredox peak appearance (approximately rectangular shape) (Figure 1g), indicating that the electrochemical interaction is controlled by capacitive charging and discharging of the electrode–electrolyte double layer. Electrodes made from nitric-acid-treated CNTs showed a more resistive phase angle (closer to  $0^\circ$ ) compared to those from nontreated CNTs (Figure 1f). This indicates a reduced

imaginary component caused by the increased surface area and double-layer capacitance. Electrodes made from nitric-acid-treated CNT fibers with a diameter as small as  $5\ \mu\text{m}$  (total electrode diameter  $\sim 10\ \mu\text{m}$ ) showed impedance values as  $709.78 \pm 64.26\ \text{k}\Omega$  (mean  $\pm$  SEM,  $n = 8$ ) at 1 kHz (Figure 1e). This value falls within the range ( $\sim 50\ \text{k}\Omega$  to  $5\ \text{M}\Omega$ ) normally used for *in vivo* neural recordings.

The CNT fiber electrodes also showed a larger cathodal charge storage capacity ( $\text{CSC}_c$ ) than the PtIr electrodes ( $278.21 \pm 5.42\ \text{mC}/\text{cm}^2$ , untreated and  $419.87 \pm 73.04\ \text{mC}/\text{cm}^2$ , treated with nitric acid vs  $2.36 \pm 0.36\ \text{mC}/\text{cm}^2$ , mean  $\pm$  SEM,  $n = 8$  for each type of electrode). The  $\text{CSC}_c$  was calculated as the time integral of the cathodic current in CV over a potential range from  $-0.6$  to  $0.8\ \text{V}$ . We further characterized the charge injection limit (CIL) of the CNT fiber and PtIr microelectrodes from voltage transient measurements. The CIL is defined as the maximum charge that can be injected in a current-controlled stimulation pulse without polarizing an electrode beyond the potentials for reduction or oxidation of water.<sup>20</sup> We estimated CIL using a conservative negative polarization potential of  $-0.6\ \text{V}$  as the threshold (Figure S1). The CNT fiber microelectrodes showed a CIL of  $3.52 \pm 0.15\ \text{mC}/\text{cm}^2$  (mean  $\pm$  SEM,  $n = 8$ , untreated) and  $5.04 \pm 0.22\ \text{mC}/\text{cm}^2$  (mean  $\pm$  SEM,  $n = 8$ , treated with nitric acid), much higher than that of the PtIr electrodes ( $0.15 \pm 0.01\ \text{mC}/\text{cm}^2$ , mean  $\pm$  SEM,  $n = 8$ ) (Figure 1h). These results indicate improved electrochemical interfacial properties of the CNT fiber electrodes compared to PtIr electrodes, making the CNT fiber electrodes an excellent candidate for both recording and stimulating electrodes for most applications.<sup>20</sup> We believe the high CIL arises from the high surface area of the CNT fiber electrode recording sites accessible to ions due to their porous microstructure.

We calculated the bending stiffness of the CNT fiber electrodes of different diameters. (See the Experimental Section for details.) The calculation gave a bending stiffness per width of  $\sim 8.16 \times 10^3\ \text{nN m}$  and  $\sim 1.58 \times 10^2\ \text{nN m}$  for electrodes made from  $20$  and  $5\ \mu\text{m}$  diameter CNT fibers, respectively (both with  $2.5\ \mu\text{m}$  thick Parylene-C insulation). This is much smaller than that of PtIr electrodes ( $\sim 1.53 \times 10^5\ \text{nN m}$ ,  $25\ \mu\text{m}$  PtIr diameter) and that reported for electrodes made of a  $7\ \mu\text{m}$  diameter carbon fiber ( $\sim 3.9 \times 10^4\ \text{nN m}$ ) or silicon probe ( $4.6 \times 10^5\ \text{nN m}$ ), although orders of magnitude higher than the values reported for the state-of-art ultrathin-polymer-based soft electrodes and that of neural tissues ( $\sim 0.1\ \text{nN m}$ ).<sup>11,12,16,21</sup>

The high softness of the CNT fiber electrodes mechanically precluded their self-supported penetration through brain tissue. We used a shuttle-assisted strategy to implant the CNT fiber electrodes to the desired depth in the brain. Briefly, individual CNT fiber electrodes were attached to tungsten wires of  $\sim 50\ \mu\text{m}$  diameter using poly(ethylene oxide) (PEO) adhesive. After the electrode/shuttle complex was inserted into the target position, the PEO dissolved and the tungsten wire shuttle device was retracted, leaving only the soft CNT fiber electrode inside the brain. Because the PEO adhesive dissolves within a few minutes from the start of implantation, the insertion process was always completed in  $\sim 2\ \text{min}$ . This resulted in an  $\sim 80\%$  rate for successful implantation to the desired depth. The most prevalent failure mode is the separation between the CNT fibers and tungsten wire shuttles before achieving the target depth, which can be maximally avoided by using enough PEO adhesive and controlling the

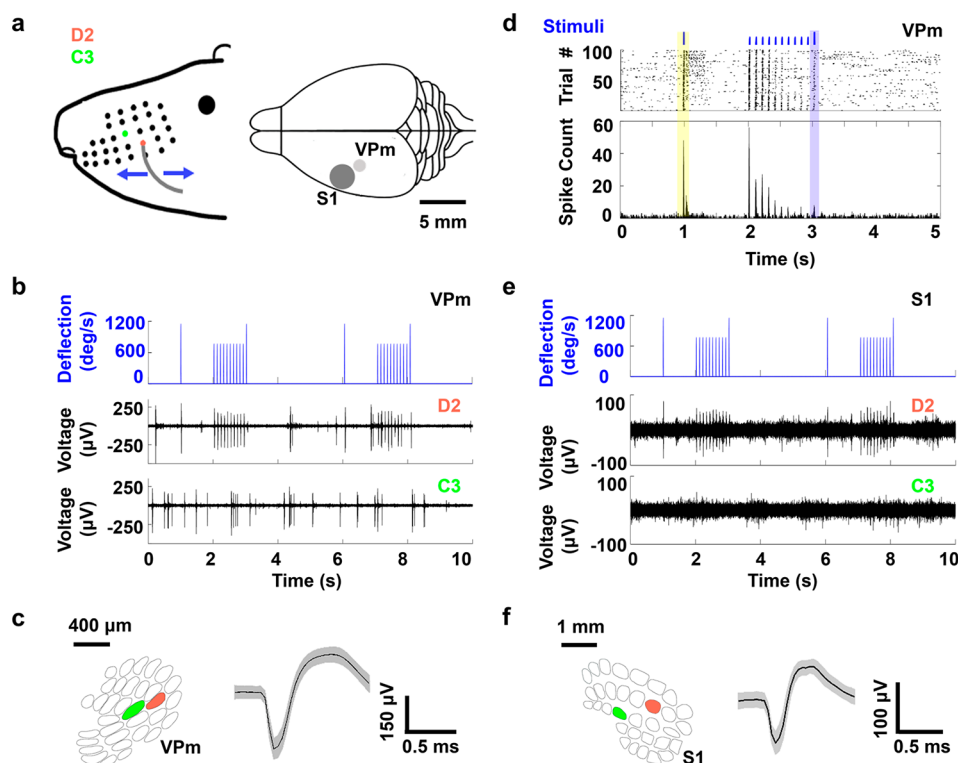


**Figure 2.** Acute neural recording with CNT fiber electrodes. (a) Left, schematic diagram of whisker deflection. Individual vibrissa was deflected in the rostral-caudal plane using a computer-controlled piezoelectric bending actuator. D2 and C3 whiskers are labeled in red and green, respectively. Right, schematic drawing showing the relative position of S1 and thalamic VPm. (b) Representative recordings from VPm with an electrode made of a 15  $\mu\text{m}$  diameter CNT fiber, in response to controlled deflection of individual vibrissa. Top trace shows the pattern of two consecutive cycles of deflections, which evokes a clearly defined and strong spiking activity when applied to the D2 whisker (middle) and no obvious response when applied to the C3 whisker (bottom). (c) Left, schematic diagram of whisker barreloid arrangement in VPm. D2 and C3 barreloids are labeled in red and green, respectively. Right, an isolated single-unit waveform from recordings in the thalamic VPm in response to D2 whisker deflection (as in the middle trace of panel b). Gray band denotes  $\pm 1$  SD. (d) Raster plot and PSTH (1 ms bin size) for the single unit isolated from recordings in the thalamic VPm in response to D2 whisker deflection (the one shown in panel c) for 100 cycles of the vibrissa deflections. One cycle of deflections is shown and aligned with the raster plot and PSTH in the top. The neuronal response to the second 1200 deg/s deflection (marked by blue box), which was preceded by 10 persistent periodic vibrissa deflections, was significantly reduced compared to that under the first 1200 deg/s deflection (marked by yellow box), consistent with the adaptation of the response profile of the VPm neurons. (e) Representative recordings from the vibrissa region of S1, in response to controlled deflection of the individual vibrissa with an electrode made of a 5  $\mu\text{m}$  diameter CNT fiber. Same stimulation pattern as panel b was applied (top), which evokes significant spiking activities when applied to the D2 whisker (middle) and no observable spiking activities when applied to the C3 whisker (bottom). (f) Left, schematic diagram of whisker barrel arrangement in S1. D2 and C3 barrels are labeled in red and green, respectively. Right, an isolated single-unit waveform from recordings in the S1 in response to D2 whisker deflection (as in middle trace of panel e). Gray band denotes  $\pm 1$  SD.

time used for insertion. The overall insertion footprint was determined by the total size of the electrode/shuttle complex and was comparable to conventional stiff microwire electrodes. A smaller shuttle device such as a carbon fiber could be used to further decrease the surgical footprint. There is strong evidence that glial scarring and the encapsulation and eventual isolation of implanted microelectrodes are primarily a result of interaction between chronic implants and brain tissue, and not due to acute injury from the implantation process.<sup>10,22</sup> Hence, we believe that the temporary use of the stiff shuttle device during the insertion would not compromise the high biocompatibility of the soft CNT fiber electrodes.

Although testing the functional viability of the electrodes could be achieved through recording anywhere throughout the brain, it is advantageous to record from well-studied areas for validation against published electrophysiological recordings. Further, validation in a sensory region of the brain provides a simple, controlled framework where action potentials can be causally induced through sensory stimulation, as compared to relying on spontaneous activity. We performed acute neural

recordings from a rat ventral posteromedial (VPm) nucleus of the thalamus and primary somatosensory cortex (S1) under whisker stimulation (Figure 2a) to test the CNT fiber electrode's capability of precisely targeting and recording from specific brain regions, and to evaluate the recording capability in deep brain structures. All of the reported measurements here were performed within 0.5–2 h post-implantation. In a typical test, a CNT fiber electrode was inserted into the VPm region of the thalamus of the rat. Whiskers on the contralateral side of the implantation site were deflected in a controlled manner using a whisker stimulation system (see the Experimental Section). Each cycle of stimulation consisted of a 1200 deg/s deflection, followed by a stimulation pulse train at 10 Hz, which included ten 900 deg/s deflections and one 1200 deg/s deflection (top, Figure 2b). The CNT fiber electrode recorded clearly defined and strong spiking activity when the stimulations were applied to the whisker D2 (middle, Figure 2b), which was identified as the primary corresponding vibrissa, while the stimulation of other whiskers were associated with either much weaker signal



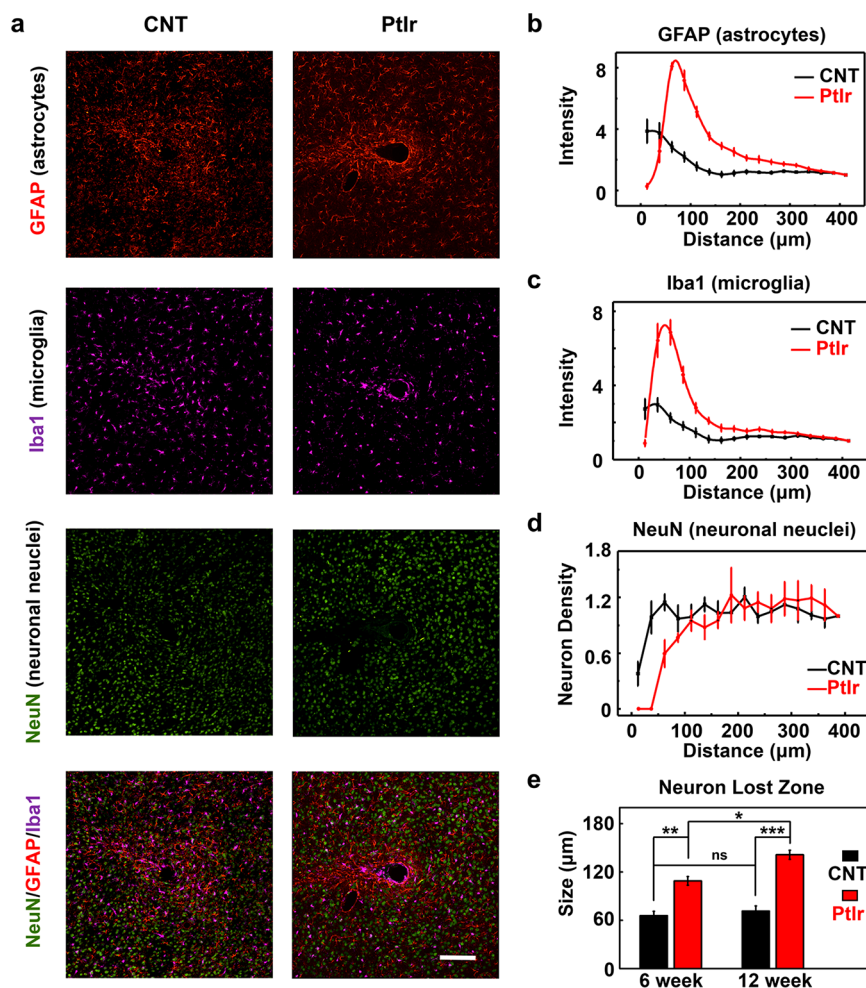


**Figure 3.** Histological studies of brain tissue reaction to chronically implanted CNT fiber microelectrodes. (a) Immunofluorescence images of tissue responses following a 6 week implantation of an electrode made from a 20  $\mu\text{m}$  diameter CNT fiber (left) and an electrode made from a 25  $\mu\text{m}$  diameter PtIr wire (right). The Parylene-C insulation layer is  $\sim 2.5$   $\mu\text{m}$  thick. The CNT fiber and Pt electrodes were implanted contralaterally in the same rat. The tissue was labeled for astrocytes (red), microglia (purple), and neurons (green). Scale bar, 100  $\mu\text{m}$ . (b, c, d) Normalized fluorescence intensity (b, c) and neuron density (d) profile as a function of distance from the center of the electrode tract, which is set as  $x = 0$   $\mu\text{m}$ , for 6 week postimplantation. Error bars show SEM ( $n = 6$ ). (e) Neuron lost zone diameters for CNT fiber and PtIr electrode implants for 6 week and 12 week postimplantation. Error bars show SEM,  $n = 6$ . \*\*\* $p < 0.001$ , \*\* $p < 0.01$ , \* $p < 0.05$ , ns,  $p > 0.05$ , one-way ANOVA.

patterns or no obvious response (bottom, Figure 2b), suggesting a precise and localized response measurement. In this example, a single-unit spike with a valley-to-peak amplitude of 372  $\mu\text{V}$  and a signal-to-noise ratio (SNR) of  $\sim 30$  was detected from the D2 whisker deflection-induced activity (Figure 2c). The raster plot and peri-stimulus time histogram (PSTH) of this unit are shown in Figure 2d. It was observed that the neuronal response to the second 1200 deg/s deflection (marked by blue color), which was preceded by 10 persistent periodic vibrissa deflections, was significantly reduced compared to that in response to the first 1200 deg/s deflection (marked by yellow). This indicates the adaptation of the response profile of the VPM neurons to persistent, ongoing sensory stimuli, a phenomenon extensively studied in literature.<sup>23,24</sup> In addition, we found that the CNT fiber electrodes implanted via the shuttle-assisted method, including those with a diameter down to  $\sim 10$   $\mu\text{m}$  ( $\sim 5$   $\mu\text{m}$  diameter CNT fibers), can robustly record spiking activity from various cortical and subcortical regions in acute settings (Figure 2e and Figures S2 and S3). These results demonstrate the capability of the CNT fiber electrodes to precisely target specific brain

regions and record single-unit neural signals with a high SNR, thus providing at least comparable brain activity recordings to those of conventional probes, but with the advantage of being chronically much more biocompatible and more MRI compatible, as will be discussed below. It is noted that the recordings with electrodes made from 5 and 15  $\mu\text{m}$  diameter CNT fibers showed comparable noise levels (Figure S4) and recording capability (Figure 2 and Figure S3). However, the insertion of electrodes from 5  $\mu\text{m}$  diameter CNT fibers was associated with a lower success rate than those from larger diameter CNT fibers. Hence, in the current work, we focus on using electrodes from larger diameter (15 and 20  $\mu\text{m}$ ) CNT fibers for histology studies and chronic recordings.

In a different set of experiments, we performed post-mortem histology 6 and 12 weeks after implantation to evaluate the brain tissue reaction to chronically implanted CNT fiber microelectrodes. PtIr microelectrodes of a similar diameter implanted contralaterally in rat brains were used for comparison. Glial encapsulation and neuronal death in the vicinity of the recording electrodes have been implicated as main factors negatively impacting the stability and longevity of

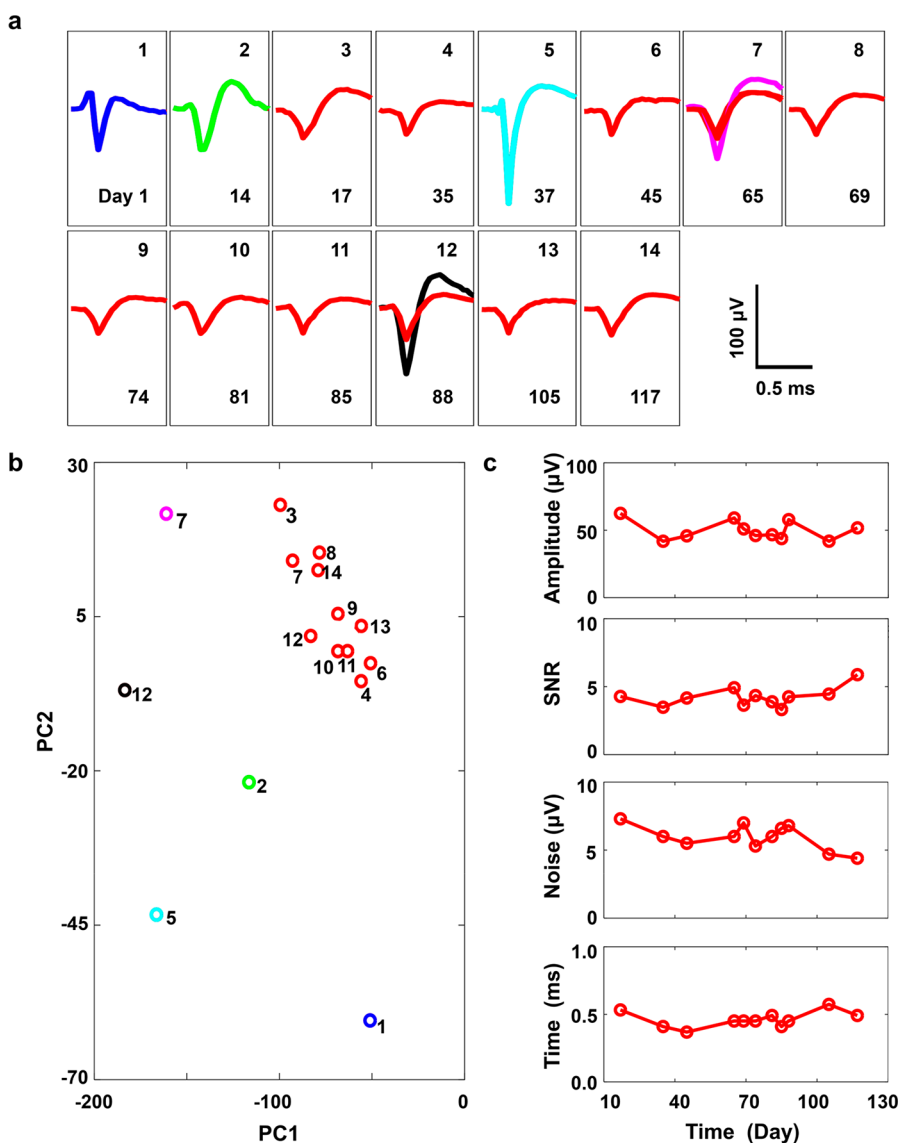


**Figure 4.** Chronic neural recording with CNT fiber electrodes. (a) Mean waveforms of units detected and isolated from day 1 to day 117 postimplantation with an electrode made of an  $\sim 15 \mu\text{m}$  diameter CNT fiber. The waveforms are isolated and averaged from 3 to 9 min recording segments. The numbers in the right top corners indicate the measurement sessions, while the numbers in the right bottom indicate days postimplantation. The units in red indicate those forming a cluster in the PCA analysis in panel b. (b) Mean PCA of waveforms recorded at different times. The principal component 1 (PC1) and principal component 2 (PC2) of each unit shown here are the average of the PC1 and PC2 of all waveforms of each unit. Numbers mark the measurement session of each unit. The same color coding is used as that in panel a. (c) Valley-to-peak amplitude and time, noise level, and SNR of the clustered single-units (the ones with red color in panels a and b), as a function of time.

chronic neural recordings.<sup>7,8</sup> The 6 week-postimplantation data (Figure 3) shows that there was a 2-fold reduction in the accumulation of astrocytes and expression of general microglia at the CNT fiber microelectrode sites (Figure 3a–c) compared to PtIr microelectrodes, indicating an overall reduction in the extent of gliosis. The loss of neurons was found to be confined within a region of approximately  $66 \pm 5 \mu\text{m}$  diameter (mean  $\pm$  SEM,  $n = 6$ ) for CNT fiber electrodes, compared to  $109 \pm 5 \mu\text{m}$  (mean  $\pm$  SEM,  $n = 6$ ) for PtIr electrodes (Figure 3a,d,e). The neuron lost zone for CNT fiber electrodes is comparable to the implantation footprint ( $\sim 20 \mu\text{m}$  diameter CNT fiber insulated with  $\sim 2.5 \mu\text{m}$  thick Parylene-C plus  $\sim 50 \mu\text{m}$  tungsten microwire shuttle), indicating that there was no obvious further neuronal degeneration after the acute tissue damage from the implantation. From the 12 week-postimplantation data (Figure S5), it can be seen that there was still

an  $\sim 1.7$ -fold reduction in GFAP (astrocytes) signal around the CNT fiber electrodes than the PtIr electrodes. The Iba1 (microglia) signal level was significantly reduced for both types of electrodes compared to the 6 week-postimplantation data and became comparable between them. The size of the neuron lost zone increased to  $\sim 1.3$ -fold around the PtIr electrodes compared to the 6 week-postimplantation data, indicating progressive neuronal degeneration, whereas no statistically significant difference was found in the neuron lost zone size between the 6 and 12 week-postimplantation results for the CNT fiber electrodes, indicating that neither neuron recovery nor further neuron loss occurred. These histological data demonstrate the ability of the CNT fiber microelectrodes to have an improved and more stable microenvironment in neural interfaces than the stiff metal electrodes. It has been suggested previously that both size and mechanical compliance play a

role in the extent of glial scarring and neural degeneration around brain implants.<sup>11–13,25</sup> Since the CNT fiber electrodes and PtIr electrodes used here have a similar diameter, the higher biocompatibility of the CNT fiber electrodes suggests the contribution of their mechanical compliance to the stable interface with the brain.

We found that the CNT fiber electrodes are capable of performing stably and continuously detecting high-quality single-unit neural signals from rats for up to 4–5 months. All chronic recordings were performed on anesthetized animals and from spontaneous neuron firing. Figure 4 and Figures S7 and S8 show a representative chronic recording result from a rat with an electrode made from a 15  $\mu\text{m}$  diameter CNT fiber implanted in the thalamus. Some other examples of chronic recording for 4–5 months with CNT fiber electrodes are shown in Figure S9. In the example shown in Figure 4, the electrode detected and isolated single-unit spikes reliably over this 4-month period (Figure 4a, Figure S7). Combined principal component analysis (PCA) of sorted spikes from measurements at different times showed that the spikes from day 17 (no. 3) to day 117 (no. 14) (marked by red) formed a cluster with close positions in the first and second principal component plane (PC1, PC2) (Figure 4b, Figure S8). The unit centers' average position shift between consecutive measurements was equivalent to 2.90  $\sigma$  of the average cluster distribution. (See the Experimental Section for details of the calculation.) The position shift for spikes from day 65 (no. 7) to day 88 (no. 12) was calculated to be 1.05  $\sigma$ . The close principal components in this largely overlapping cluster suggests a possibility that these units, especially those spikes recorded from day 65 (no. 7) to day 88 (no. 12), were generated by the same neuron, which remained in close proximity to the electrode for this duration of the chronic recording, as indicated by the persistently high SNR of these units (Figure 4c). However, the confirmation on if they were from the same neuron needs more evidence and warrants further studies in the future. In addition, the stable valley-to-peak amplitude throughout this 4-month period (Figure 4c) was distinct from previous neuron probes where decreasing amplitudes were always observed along with the increase of implantation time.<sup>26,27</sup> These recording results, together with the histological studies, strongly indicated that a more stable interface was formed between the soft CNT fiber electrodes and brain tissues. The 4–5 month recording period provides a useful window into studying phenomena such as plasticity, development, and learning. We also observed the appearance and disappearance (and possibly reappearance) of some single-unit signals on day 37, 65, and 88. Since the recording was performed on anesthetized animals and from spontaneous neuron firing, one possible reason for this instability was because of the switching between firing and silencing of the neurons, due to different depths of anesthesia.<sup>28–32</sup> The firing rate of the detected spikes, even those forming the cluster, showed a large variation on different days (Figure S10), which may also reflect the instability in spontaneous firing activity due to the difference in anesthesia depth.

It was reported that the state-of-art ultrathin-polymer-based soft electrodes with a stiffness comparable to that of neural tissues, could form glial-scar-free and seamless integration with the brain tissue,<sup>13,33</sup> and stably record single-unit signals as well as track the same neurons in mouse brains for at least 8 months without probe repositioning.<sup>13</sup> Different from these ultrasoft electrodes, a very slight gliosis around the CNT fiber

electrodes was observed at similar time points postimplantation. The neuron lost zone around the CNT fiber implants was found to be nearly constant and confined in a small region of  $\sim 60\text{--}70\ \mu\text{m}$  in size, with neither recovery nor further neuron loss observed. This is also different from previous studies, which showed a significant neuron recovery around the ultrasoft mesh electrodes.<sup>13</sup> The fact that no dense glial scar formed around the CNT fiber electrodes, and that the neurons were within the recording distance from the CNT fiber electrodes, provides mechanistic support for our stable chronic neural recordings. Chronic *in vivo* monitoring of the electrode impedance could provide useful information on the interfacial stability. Unfortunately, the recording system we used was not equipped with the *in vivo* impedance measurement module, which made this data unavailable. Whether the CNT fiber electrodes can track the same neurons in chronic time scales and how the recording capability as well as the interface between the CNT fiber implants and brain tissue evolves over longer term implantation (on the order of years) warrant further research. In addition, the statistics data from a larger number of chronic recordings (more electrodes and more animals) will be important to further evaluate the overall performance of the CNT fiber electrodes.

The CNT fiber microelectrodes have a high tensile strength, which can be retracted and moved after insertion, providing a solution to overcome many challenges faced with the fixed implantable microelectrodes. Movable stiff microelectrodes were used to break through the glial sheath surrounding the microelectrodes to seek fresh tissue and restore the electrical interface with functional neurons in long-term experiments.<sup>34</sup> For soft electrodes, which are associated with greatly reduced inflammatory responses, the ability to fine-tune the geographical position of the microelectrode after implantation can offer advantages in both neural recording and stimulation:<sup>35,36</sup> (1) selecting cells with particular response properties, (2) seeking neurons that might have been silent during the time of insertion, (3) monitoring changes in a small population of single neurons undergoing neuronal plasticity, (4) seeking neurons for simultaneous monitoring of pairs and triplets to probe neuronal tracts and connectivity, and (5) recording from more than one brain region with individual electrodes such as from neurons in banks of sulci where the neurons are located at multiple different depths along the banks of sulci.

We demonstrated the capability of the CNT fiber microelectrodes to form movable neural interfaces by manually moving them upward along the axial direction postinsertion in acute recordings, as shown in Figure S11. In a typical recording, a CNT fiber microelectrode was fast-inserted into the brain of an anesthetized rat to a predetermined ventral posterolateral thalamic nucleus (VPL) region using the shuttle-assisted strategy described as above. After the shuttle device was removed, the CNT fiber electrode was manually retracted to five different depths (from  $-6838$  to  $-2160\ \mu\text{m}$  relative to the dura mater) spanning from the VPL to the primary somatosensory region associated with the trunk (S1Tr) region (Figure S11a),<sup>37</sup> using a hydraulic micropositioner with a submicron resolution. An electrophysiological recording was conducted at each depth. All recordings show clearly defined spiking activities (Figure S11b), with single-unit spike waveforms detected and isolated from each recording as shown in Figure S11c. The high-quality recording at different depths indicates that moving the CNT fiber electrode did not cause disturbance to neurons in close proximity to the



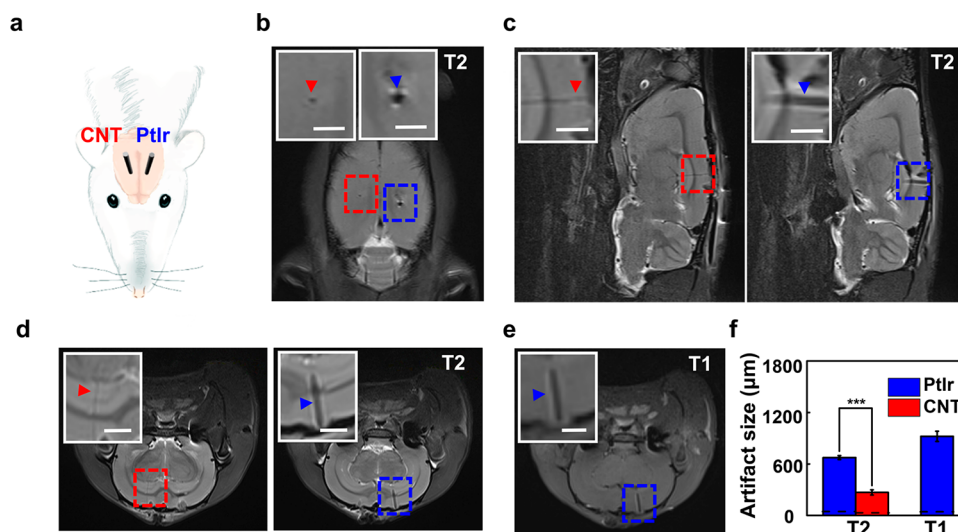


**Figure 5.** *In vivo* MRI artifact assessment. (a) Schematic diagram of a rat implanted contralaterally with a CNT fiber and PtIr microwire used for MRI studies. (b–d) Horizontal (b), sagittal (c), and coronal (d) sections of the T2-weighted images of a rat implanted contralaterally with a Parylene-C-insulated CNT fiber and PtIr microwire. The insets are zoomed-in photographs of the red or blue boxes. Scale bar, 1.5 mm. The CNT fiber and PtIr microwire are in different planes in the sagittal and coronal images. (e) Coronal section of the T1-weighted image of the rat implanted contralaterally with a Parylene-C-insulated CNT fiber and PtIr microwire. The red and blue dashed boxes/arrows mark the CNT fiber and PtIr microwire, respectively. (f) MRI artifact size of the Parylene-C-insulated CNT fibers and PtIr microwires. The black dashed line denotes their actual size. CNT fibers are invisible in T1-weighted images. Error bars denote SEM,  $n = 5$ . \*\*\* $p < 0.001$ ; one-way ANOVA. All CNT fibers and PtIr microwires used here are insulated with  $\sim 2.5 \mu\text{m}$  Parylene-C.

electrode (as indicated by the large spike amplitude). The above result demonstrates that the tensile strength of the CNT fiber electrodes is high enough to enable them being moved postimplantation inside the brain to form adaptive neural interface while retaining a high softness for enhanced neural integration over chronic time scales. In the future, the integration of motorized microdrives with the CNT fiber electrodes assembly may enable autonomous and reliable fine-tuning of the position of the recording sites in freely behaving animals, which will benefit many basic neurophysiological studies.

A high MRI compatibility with a reduced artifact from implanted electrodes is critical for combining electrophysiology and anatomical/functional MRI mapping. Previous work investigated the artifact properties of a 1.5 mm long, 1.3 mm diameter cylindrical surface made of CNT fibers (by wrapping the CNT fibers onto a polyurethane tube) under 3 T MRI scanning, which showed that the CNT fiber cylinder had an artifact with the size reduced as much as 62% and 74% on gradient echo (GE) and spin echo (SE) images, respectively, compared to the PtIr cylinder.<sup>38</sup> Here we characterized the MRI image artifacts of single CNT fiber electrodes implanted into rat brains using a 7.0 T MR scanner (Bruker BioSpin MRI, Germany), in comparison to PtIr microwire electrodes with a similar diameter implanted contralaterally as schematically shown in Figure 5a. The electrodes made from  $20 \mu\text{m}$  CNT fibers resulted in an artifact size of  $268.4 \pm 29.9 \mu\text{m}$  (mean  $\pm$  SEM,  $n = 5$ ), compared to  $675.1 \pm 22.5 \mu\text{m}$  (mean  $\pm$  SEM,  $n = 5$ ) of PtIr electrodes in T2 anatomical images (Figure 5b–d,f), as measured using an edge detecting method illustrated in Figure S13. In T1-weighted images, the PtIr electrodes produced a  $922.5 \pm 59.2 \mu\text{m}$  (mean  $\pm$  SEM,  $n = 5$ ) artifact, while the artifact associated with the CNT fiber electrode is barely visible (Figure 5e). These results indicate greatly reduced magnetic field distortion by the CNT fiber electrode implants as compared to the PtIr electrode implants. The

greatly reduced artifact size of the CNT fiber electrodes enables visualization of the brain tissues in a closer vicinity of the electrodes. This is important for a wide range of applications including verification of electrode placement and postoperative assessment and identification of pathological abnormalities related (e.g., hemorrhage) or nonrelated to DBS, such as a tumor and stroke.<sup>39–41</sup>

The variation of magnetic susceptibility between the implants and surrounding tissues is usually considered the dominant cause for the MRI artifacts of the implanted electrodes.<sup>42</sup> The PtIr electrodes induce severe field distortions with a relatively large paramagnetic susceptibility of  $\sim 231 \text{ ppm}$ <sup>38</sup> and  $\Delta\chi \approx 240 \text{ ppm}$  with respect to that of water ( $\chi = -9.05 \text{ ppm}$ ). Carbon in graphite form has a highly anisotropic diamagnetic susceptibility, with susceptibility orthogonal to the atomic layers 70 times greater than that parallel to the layers ( $\chi = -8.5 \text{ ppm}$ ), which is very close to that of water.<sup>1,42</sup> CNT fibers are estimated to have a diamagnetic susceptibility of approximately  $-26 \text{ ppm}$ .<sup>43</sup> Due to the dependence of the magnetic susceptibility on the growth and treatment conditions, as well as the structure of the CNT fibers, the exact value of magnetic susceptibility of our CNT fibers could be different from this estimation. However, the greatly reduced artifact size suggests a closer value to that of water than PtIr. In comparison with the G-Cu electrodes reported previously, the CNT fiber electrodes of a  $20 \mu\text{m}$  diameter showed a larger artifact in T2 anatomical images than the G-Cu electrodes of a  $100 \mu\text{m}$  diameter, indicating less MRI compatibility than G-Cu electrodes.<sup>1</sup> This is understandable considering the much closer magnetic susceptibility between copper ( $-9.63 \text{ ppm}$ ) and water. In addition, although there should be no major iron catalyst residue contamination in the CNT fibers used here owing to the base-growth mode of the CNTs, which left most catalysts at the bottom/outside of the CNT array,<sup>44,45</sup> there might be a slight iron catalyst residue in CNT fibers, which could compromise their MRI compatibility compared to



copper. Eddy currents induced in conductive implants by gradient switching and RF field accounts for another source of MRI artifacts of the implantable electrodes.<sup>46</sup> We have calculated the eddy currents (Supporting Information) and found that due to the small geometrical size and area receiving the magnetic flux the induced eddy current in CNT fiber electrodes is quite small and decays fast, hence contributing little to the artifacts.<sup>38,47</sup>

Our results demonstrate that the soft CNT fiber electrodes are capable of reliably detecting high-quality single-unit neural signals for up to 4–5 months. Although not as soft as the state-of-art ultrathin-polymer-based electrodes, and the demonstrated chronic recording period was not as long either, several features of the CNT fiber electrodes make them unique and desirable for many studies. First, the fabrication of the CNT fiber electrodes, similar to that of conventional metal microwire electrodes, does not involve the photolithographic process. Together with the easily implemented shuttle-assisted implantation process, this makes the CNT fiber electrodes readily applicable to neuroscience laboratories. Second, the improved electrochemical interfacial properties of the CNT fibers compared to metal allow for miniaturization of the electrode active site size without compromising the recording capability or stimulation efficacy. We show here that electrodes with an active site size as small as 5  $\mu\text{m}$  can record high-quality single-unit signals, compared to the tens of microns active site size in metal electrodes. A small active site size can not only improve the stimulation resolution and selectivity<sup>48</sup> and benefit single neuron discrimination in recordings,<sup>49</sup> especially from small and densely packed cells,<sup>36</sup> but also is necessary for developing intracellular probes for *in vivo* neural recordings in the future. We believe that these features, together with the MRI compatibility and capability for stable chronic neural electrical interfacing, provide the soft CNT fiber electrodes unique research capabilities to impact both basic neurophysiological studies and emerging neural prosthetic technologies. For future development, the implantation method, which is more tolerant on the insertion process and time, will be beneficial for the applications of the CNT fiber electrodes. In addition, in this study, we have only demonstrated the electrophysiological recordings from single CNT fiber electrodes and the development of the CNT fiber electrode array for multiplexed neural interfacing will be important for future studies to extend the application of the soft and MRI compatible CNT fiber electrodes.

## ■ ASSOCIATED CONTENT

### 📄 Supporting Information

The Supporting Information is available free of charge on the ACS Publications website at DOI: [10.1021/acs.nanolett.8b04456](https://doi.org/10.1021/acs.nanolett.8b04456).

Experimental details, voltage transient measurement, acute neural recordings, noise level comparison, 12 week postimplantation histological studies, procedure of defining probe tract center, superimposed detected unit activities from chronic recordings, boxplots of PC1 and PC2 of waveforms, other examples of chronic neural recording, firing rate of the isolated single units, multidepth recording and PSD analysis, and MRI artifact size measurement, and parameters used for bending stiffness calculation (PDF)

## ■ AUTHOR INFORMATION

### Corresponding Authors

\*E-mail: [garrett.stanley@bme.gatech.edu](mailto:garrett.stanley@bme.gatech.edu).

\*E-mail: [xjduan@pku.edu.cn](mailto:xjduan@pku.edu.cn).

### ORCID

Xiaojie Duan: 0000-0001-7799-3897

### Author Contributions

X.D., L.L., and X.F. conceived and designed the experiments. L.L., Y.Z., J.Z., D.L., and Q.L. grew the CNT array and spun the CNT fibers. L.L., X.F., S.Z., and Z.X. fabricated and characterized the electrodes. L.L., X.F., and Y.L. performed the acute and chronic neural recordings and data analysis, L.L., X.F., and S.Z. performed the histology and MRI studies. X.D. and G.S. supervised the project. X.D., L.L., X.F., and G.S. wrote the manuscript. All of the authors discussed the results and commented on the manuscript.

### Author Contributions

The authors declare no competing interests.

### Notes

The authors declare no competing financial interest.

## ■ ACKNOWLEDGMENTS

We thank Dr. Shaowu Li and Dr. Song Yang from the Functional Neuroimage Department, Beijing Neurosurgical Institute, and the Core Facilities at the School of Life Sciences, Peking University, for help in magnetic resonance imaging and for assistance with confocal microscopy, respectively. X.D. acknowledges the support by grants from the National Natural Science Foundation of China (21422301 and 91648207), the National Basic Research Program of China (2016YFA0200103 and 2014CB932500), Beijing Graphene Innovation Program (Z161100002116028), and China's 1000 Young Talent Award program.

## ■ REFERENCES

- (1) Zhao, S.; Liu, X.; Xu, Z.; Ren, H.; Deng, B.; Tang, M.; Lu, L.; Fu, X.; Peng, H.; Liu, Z.; et al. *Nano Lett.* **2016**, *16* (12), 7731–7738.
- (2) Logothetis, N. K.; Pauls, J.; Augath, M.; Trinath, T.; Oeltermann, A. *Nature* **2001**, *412* (6843), 150.
- (3) Figeé, M.; Luigies, J.; Smolders, R.; Valencia-Alfonso, C.-E.; Van Wingen, G.; De Kwaasteniet, B.; Mantione, M.; Ooms, P.; De Koning, P.; Vulink, N.; et al. *Nat. Neurosci.* **2013**, *16* (4), 386.
- (4) Gosselin, N.; Bottari, C.; Chen, J.-K.; Petrides, M.; Tinawi, S.; de Guise, E.; Pitto, A. *J. Neurotrauma* **2011**, *28* (3), 329–341.
- (5) Stead, M.; Bower, M.; Brinkmann, B. H.; Lee, K.; Marsh, W. R.; Meyer, F. B.; Litt, B.; Van Gompel, J.; Worrell, G. A. *Brain* **2010**, *133* (9), 2789–2797.
- (6) Fattahi, P.; Yang, G.; Kim, G.; Abidian, M. R. *Adv. Mater.* **2014**, *26* (12), 1846–1885.
- (7) Polikov, V. S.; Tresco, P. A.; Reichert, W. M. *J. Neurosci. Methods* **2005**, *148* (1), 1–18.
- (8) Winslow, B. D.; Tresco, P. A. *Biomaterials* **2010**, *31* (7), 1558–1567.
- (9) Prasad, A.; Xue, Q.-S.; Sankar, V.; Nishida, T.; Shaw, G.; Streit, W. J.; Sanchez, J. C. *J. Neural Eng.* **2012**, *9* (5), 056015.
- (10) McConnell, G. C.; Rees, H. D.; Levey, A. I.; Gutekunst, C.-A.; Gross, R. E.; Bellamkonda, R. V. *J. Neural Eng.* **2009**, *6* (5), 056003.
- (11) Kozai, T. D. Y.; Langhals, N. B.; Patel, P. R.; Deng, X.; Zhang, H.; Smith, K. L.; Lahann, J.; Kotov, N. A.; Kipke, D. R. *Nat. Mater.* **2012**, *11* (12), 1065.
- (12) Xie, C.; Liu, J.; Fu, T.-M.; Dai, X.; Zhou, W.; Lieber, C. M. *Nat. Mater.* **2015**, *14* (12), 1286.
- (13) Fu, T.-M.; Hong, G.; Zhou, T.; Schuhmann, T. G.; Viveros, R. D.; Lieber, C. M. *Nat. Methods* **2016**, *13* (10), 875.

- (14) Liu, J. Syringe Injectable Electronics. *Biomimetics Through Nanoelectronics*; Springer, 2018; pp 65–93.
- (15) Vitale, F.; Summerson, S. R.; Aazhang, B.; Kemere, C.; Pasquali, M. *ACS Nano* **2015**, *9* (4), 4465–4474.
- (16) Kim, T.-i.; McCall, J. G.; Jung, Y. H.; Huang, X.; Siuda, E. R.; Li, Y.; Song, J.; Song, Y. M.; Pao, H. A.; Kim, R.-H. *Science* **2013**, *340* (6129), 211–216.
- (17) Jia, J.; Zhao, J.; Xu, G.; Di, J.; Yong, Z.; Tao, Y.; Fang, C.; Zhang, Z.; Zhang, X.; Zheng, L.; et al. *Carbon* **2011**, *49* (4), 1333–1339.
- (18) Zhao, J.; Zhang, X.; Di, J.; Xu, G.; Yang, X.; Liu, X.; Yong, Z.; Chen, M.; Li, Q. *Small* **2010**, *6* (22), 2612–2617.
- (19) Geng, H.-Z.; Kim, K. K.; So, K. P.; Lee, Y. S.; Chang, Y.; Lee, Y. *H. J. Am. Chem. Soc.* **2007**, *129* (25), 7758–7759.
- (20) Cogan, S. F. *Annu. Rev. Biomed. Eng.* **2008**, *10*, 275–309.
- (21) Tyler, W. J. *Nat. Rev. Neurosci.* **2012**, *13* (12), 867.
- (22) Schmidt, S.; Horch, K.; Normann, R. *J. Biomed. Mater. Res.* **1993**, *27* (11), 1393–1399.
- (23) Wang, Q.; Webber, R. M.; Stanley, G. B. *Nat. Neurosci.* **2010**, *13* (12), 1534.
- (24) Whitmire, C. J.; Waiblinger, C.; Schwarz, C.; Stanley, G. B. *Cell Rep.* **2016**, *14* (4), 795–807.
- (25) Qing, Q.; Jiang, Z.; Xu, L.; Gao, R.; Mai, L.; Lieber, C. M. *Nat. Nanotechnol.* **2013**, *9* (2), 142.
- (26) Sanchez, J. C.; Alba, N.; Nishida, T.; Batich, C.; Carney, P. R. *IEEE Trans. Neural Syst. Rehabil. Eng.* **2006**, *14* (2), 217–221.
- (27) Chestek, C. A.; Gilja, V.; Nuyujukian, P.; Foster, J. D.; Fan, J. M.; Kaufman, M. T.; Churchland, M. M.; Rivera-Alvidrez, Z.; Cunningham, J. P.; Ryu, S. I.; et al. *J. Neural Eng.* **2011**, *8* (4), 045005.
- (28) Antkowiak, B.; Hentschke, H.; Kirschfeld, K. *Br. J. Anaesth.* **1997**, *79* (5), 617–624.
- (29) Antkowiak, B.; Helfrich-Förster, C. *Anesthesiology* **1998**, *88* (6), 1592–605.
- (30) Ries, C. R.; Puil, E. *J. Neurophysiol.* **1999**, *81* (4), 1795–801.
- (31) Aksenov, D. P.; Li, L.; Miller, M. J.; Iordanescu, G.; Wyrwicz, A. *M. J. Cereb. Blood Flow Metab.* **2015**, *35*, 1819–1826.
- (32) Massey, C. A.; Iceman, K. E.; Johansen, S. L.; Wu, Y.; Harris, M. B.; Richerson, G. B. *J. Neurophysiol.* **2015**, *113* (7), 2879–2888.
- (33) Luan, L.; Wei, X.; Zhao, Z.; Siegel, J. J.; Potnis, O.; Tuppen, C. A.; Lin, S.; Kazmi, S.; Fowler, R. A.; Holloway, S.; et al. *Sci. Adv.* **2017**, *3* (2), No. e1601966.
- (34) Lubenov, E. V.; Siapas, A. G. *Nature* **2009**, *459* (7246), 534.
- (35) Muthuswamy, J.; Anand, S.; Sridharan, A. *Front. Neurosci.* **2011**, *5*, 94.
- (36) Guitcount, G.; Markowitz, J. E.; Liberti, W. A.; Gardner, T. J. *J. Neural Eng.* **2013**, *10* (4), 046016.
- (37) Paxinos, G.; Watson, C. *The Rat Brain in Stereotaxic Coordinates*, 5th ed.; Academic Press, 2004.
- (38) Jiang, C.; Hao, H.; Li, L. *J. Neural Eng.* **2013**, *10* (2), 026013.
- (39) Mobin, F.; De Salles, A. A.; Behnke, E. J.; Frysinger, R. *Stereotact. Funct. Neurosurg.* **2000**, *72* (2–4), 225–232.
- (40) Finelli, D. A.; Rezai, A. R.; Ruggieri, P. M.; Tkach, J. A.; Nyenhuis, J. A.; Hrdlicka, G.; Sharan, A.; Gonzalez-Martinez, J.; Stypulkowski, P. H.; Shellock, F. G. *Am. J. Neuroradiol.* **2002**, *23* (10), 1795.
- (41) Thani, N. B.; Bala, A.; Swann, G. B.; Lind, C. R. *Neurosurgery* **2011**, *69* (1), 207–214.
- (42) Schenck, J. F. *Med. Phys.* **1996**, *23* (6), 815–850.
- (43) Likodimos, V.; Glenis, S.; Guskos, N.; Lin, C. *Phys. Rev. B: Condens. Matter Mater. Phys.* **2003**, *68* (4), 045417.
- (44) Liu, K.; Sun, Y.; Chen, L.; Feng, C.; Feng, X.; Jiang, K.; Zhao, Y.; Fan, S. *Nano Lett.* **2008**, *8* (2), 700–705.
- (45) Zhang, X.; Jiang, K.; Feng, C.; Liu, P.; Zhang, L.; Kong, J.; Zhang, T.; Li, Q.; Fan, S. *Adv. Mater.* **2006**, *18* (12), 1505–1510.
- (46) Graf, H.; Steidle, G.; Martirosian, P.; Lauer, U. A.; Schick, F. *Magnetic Resonance in Medicine. Magn. Reson. Med.* **2005**, *54* (1), 231–234.
- (47) Shenhav, A.; Azhari, H. *Magnetic Resonance in Medicine. Magn. Reson. Med.* **2004**, *52* (6), 1465–1468.
- (48) Sakas, D. E.; Simpson, B. A. *Operative Neuromodulation: Vol. 2: Neural Networks Surgery*; Springer Science & Business Media, 2007.
- (49) Woepfel, K.; Yang, Q.; Cui, X. T. *Current opinion in Biomed. Eng.* **2017**, *4*, 21–31.